

ADVANCED MATERIALS

Supporting Information

for *Adv. Mater.*, DOI: 10.1002/adma.202001324

Strong Ferromagnetism Achieved via Breathing Lattices in Atomically Thin Cobaltites

Sisi Li, Qinghua Zhang, Shan Lin, Xiahan Sang, Ryan F. Need, Manuel A. Roldan, Wenjun Cui, Zhiyi Hu, Qiao Jin, Shuang Chen, Jiali Zhao, Jia-Ou Wang, Jiesu Wang, Meng He, Chen Ge, Can Wang, Hui-Bin Lu, Zhenping Wu, Haizhong Guo, Xin Tong, Tao Zhu, Brian Kirby, Lin Gu, Kui-juan Jin, and Er-Jia Guo**

Supporting Information

Title Strong Ferromagnetism Achieved via Breathing Lattices in Atomically Thin Cobaltites

*Sisi Li, † Qinghua Zhang, † Shan Lin, † Xiahan Sang, Ryan F. Need, Manuel A. Roldan, Wenjun Cui, Zhiyi Hu, Qiao Jin, Shuang Chen, Jiali Zhao, Jia-Ou Wang, Jiesu Wang, Meng He, Chen Ge, Can Wang, Hui-Bin Lu, Zhenping Wu, Haizhong Gu, Xin Tong, Tao Zhu, Brian Kirby, Lin Gu, Kui-juan Jin, * and Er-Jia Guo**

† S. S. Li, Q. H. Zhang, and S. Lin contributed equally to this work.

* Correspondence and requests for materials should be addressed to K. J. and E. J. G. (emails: kjjin@iphy.ac.cn and ejguo@iphy.ac.cn)

This file includes:

Figure S1. SHG polarimetry of SCO single layers

Figure S2. Structural characterizations of L_3S_n superlattices

Figure S3. Structural characterizations of L_mS_1 superlattices

Figure S4. HAADF-STEM images of L_mS_n superlattices

Figure S5. ABF-STEM images for L_3S_3 and L_3S_8 superlattices

Figure S6. Electronic states of L_3S_3 and L_3S_8 superlattices

Figure S7. Magnetization characterizations

Figure S8. XRR curves of L_5S_1 and L_5S_{10} superlattices

Figure S9. PNR measurements on a L_5S_{10} superlattice

Figure S10. Microstructural characterizations of a L_1S_1 superlattice

Figure S11. Magnetization characterizations of L_mS_1 superlattices

Supplementary Notes 1, 2, and 3 (Figures S12, S13, and S14 are included)

Supplementary References

Figure S1. SHG polarimetry of SCO single layers. (a) and (d) Schematics of sample geometry for 2 u. c.- and 40 u. c.-thick SCO layers, respectively. (b) [(e)] $I_{2\omega\parallel}$ and (c) [(f)] $I_{2\omega\perp}$ were taken from a 2 u. c. [40 u. c.]-thick C-SCO [P-SCO] single layer, respectively. The solid lines in (e) and (f) represent the theoretical fittings to SHG data with m point group symmetry. However, the SHG signals from a 2 u. c.-thick C-SCO film could not be well-fitted by most of crystallographic symmetries due to the high noise level. (g) SHG signals are plotted as a function of SCO layer thickness. The SHG signals from the reflective p -polarized light were recorded when the p -polarized light incident on the sample, i.e. the “ p -in p -out” SHG signal. We observed a sharp increment of SHG signal when the SCO layer thickness beyond 5 u. c. These results indicate the SCO films exhibit a clear crystallographic symmetry transition in SCO single layers with increasing the layer thickness. Such a structural transition agrees with an earlier theoretical prediction that the infinite layered cuprates undergo an oxygen coordination transformation from a bulk-like planar-type to a chain-type structure when the layer thickness below 5 u. c. [SR1]

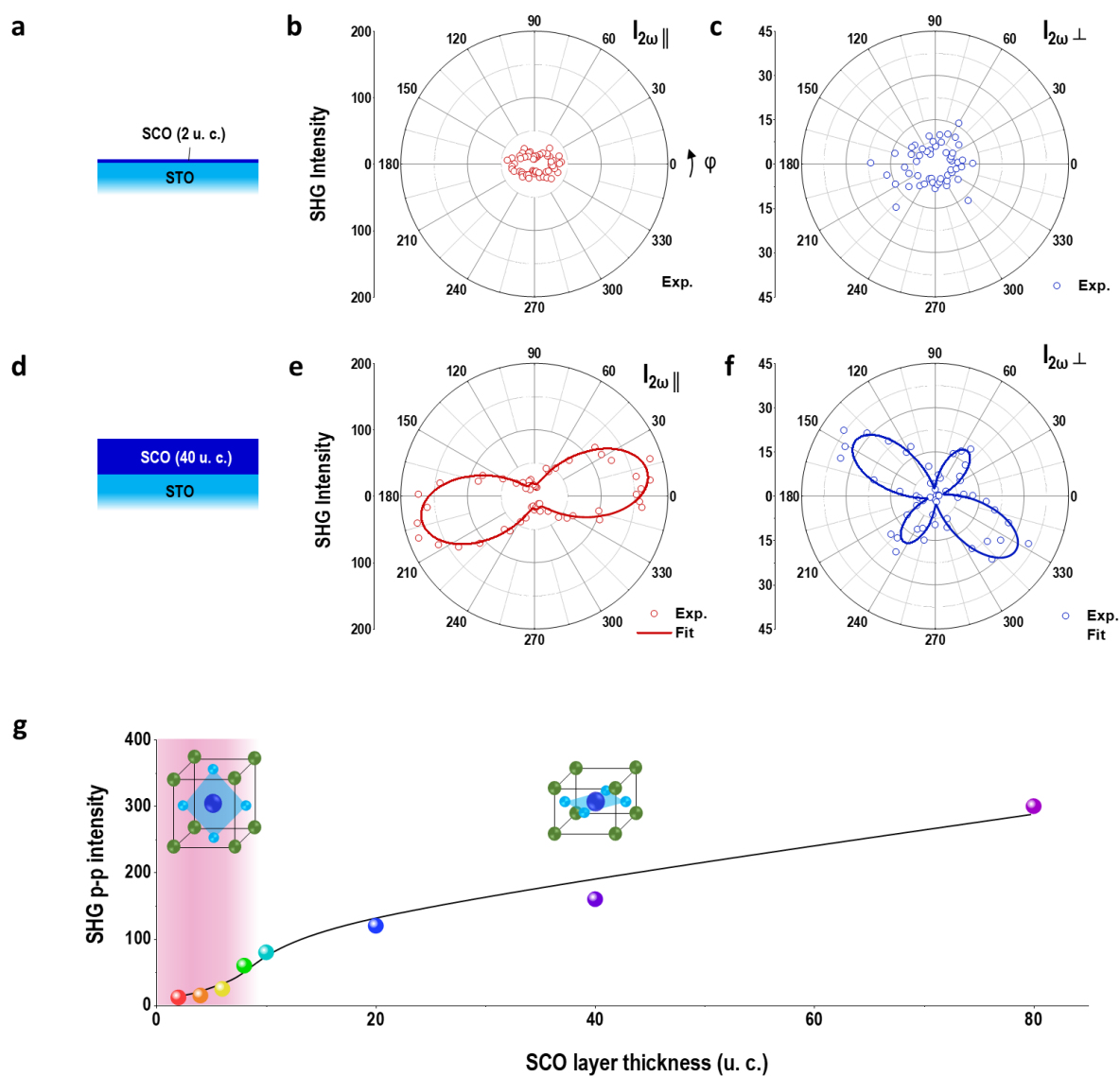


Figure S2. Structural characterizations of L_3S_n superlattices. (a) X-ray reflectivity (XRR) and x-ray diffraction (XRD) θ - 2θ scans of L_3S_n superlattices for $1 \leq n \leq 20$. XRR results indicate the well-defined interfaces and uniform chemical compositions within each superlattice. Narrow superlattice peaks and clear Kiessig fringes suggest all superlattices are epitaxially grown with extreme high quality. (b) Reciprocal space maps (RSMs) near the STO substrates' 103 reflections for L_3S_n superlattices. All superlattices are coherently strained by the STO substrates. The positions of superlattice $00l$ peaks for the L_3S_n ($n \leq 3$) are nearly unchanged. However, as increasing the SCO layer thickness beyond 5 u. c., the superlattice peaks shift sharply to the large out-of-plane reciprocal lattice vector (q_z), indicating a sudden structural transition in the SCO layers when the thickness exceeds 5 u.c. The out-of-plane lattice constants (c_{SL}) calculated from RSMs of L_3S_n superlattices are summarized in Fig. 2c of main text. (c) and (d) Rocking curves around the L_3S_1 superlattice 002 peak and STO substrate 002 peak, respectively. The full width at half maximums of SL and substrate are 0.04° and 0.02° , respectively, indicating a good crystallinity of our SLs.

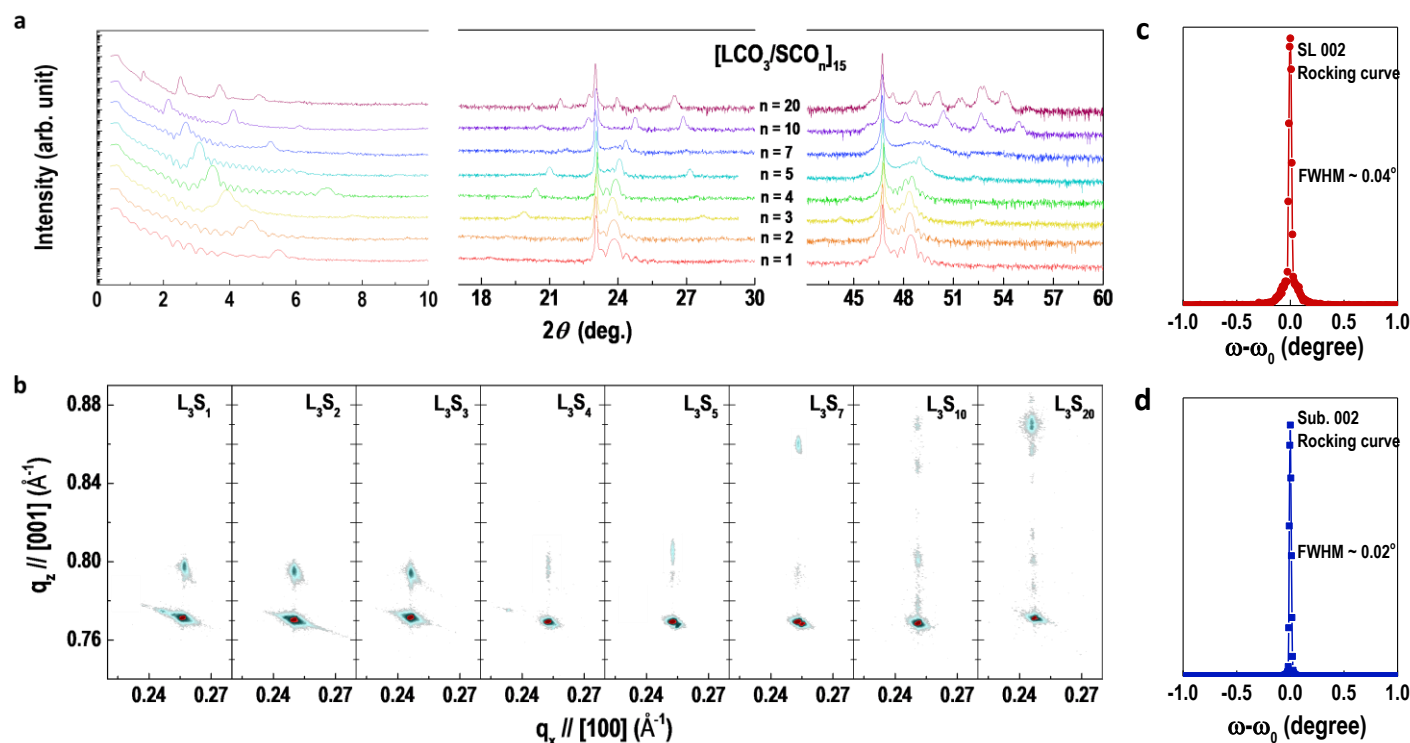


Figure S3. Structural characterizations of L_mS_1 superlattices. (a) XRR and XRD θ - 2θ scans and (b) RSMs around substrates' 103 peaks of L_mS_1 superlattices for $1 \leq m \leq 10$. In contrast to Fig. S2, the peak positions of L_mS_1 superlattices are nearly unchanged, indicated by the dashed lines in (a) and (b). These results suggest that the out-of-plane lattice constants (c_{SL}) of L_mS_1 superlattices keep nearly a fixed value, which are independent of the LCO layer thickness. The modulation of c_{SL} in the L_mS_n superlattices is dominated by the number of SCO unit cells.

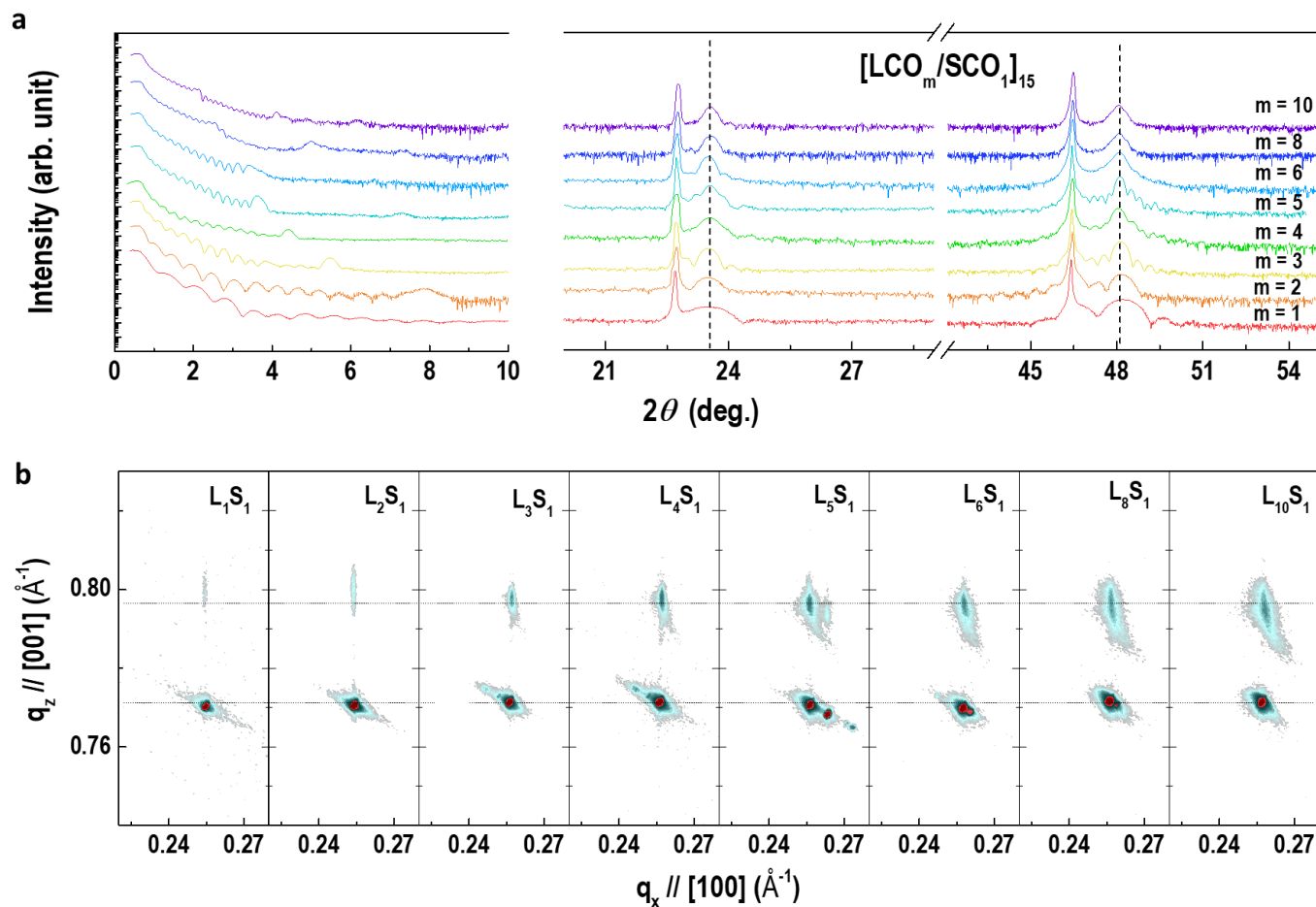


Figure S4. HAADF-STEM images of L_mS_n superlattices. Cross-sectional HAADF-STEM images of (a) L_1S_3 , (b) L_3S_3 , (c) L_5S_3 , (d) L_1S_8 , (e) L_3S_8 , and (f) L_5S_{10} . Samples are imaged along the pseudocubic [100] zone axis. In the case of HAADF-STEM images, the intensity scales roughly with the value of $Z^{1.7}$, where Z is the atomic number of elements. The brighter features correspond to the positions of heavy elements, like lanthanum ($Z = 57$) and strontium ($Z = 38$). The cobalt ($Z = 27$) and copper ($Z = 29$) atoms, occupied the dimmer spots in between the La and Sr, have similar intensities. All HAADF-STEM images indicate the interfaces between the SCO and LCO layers are atomically sharp. The chemical intermixing at interfaces is within one-unit-cell thickness. The white scale bars in each panel indicate 2 nm in length. Atomic distance between the A-site cations, i. e. out-of-plane lattice constants (c), along the [001] direction was summarized on the right side of each HAADF-STEM image. The variation range of lattice constants of LCO and SCO were indicated as red and blue shadows, respectively. Quantitative analysis of structural parameter shows that the lattice constants of SCO in the L_mS_8 ($m = 1$ and 3) and L_5S_{10} superlattices are ~ 3.45 Å, whereas that of SCO in the L_mS_3 ($m = 1, 3,$ and 5) superlattices is ~ 3.80 Å. Meanwhile, the lattice constant of LCO increases from ~ 3.78 to ~ 3.80 Å as the thickness of SCO increases from 3 to 10 u. c. The changes of LCO out-of-plane lattice constant were observed in both three samples, indicating a robust manipulation of lattice parameter in LCO induced by structural transformation in SCO as increasing the SCO layer thickness.

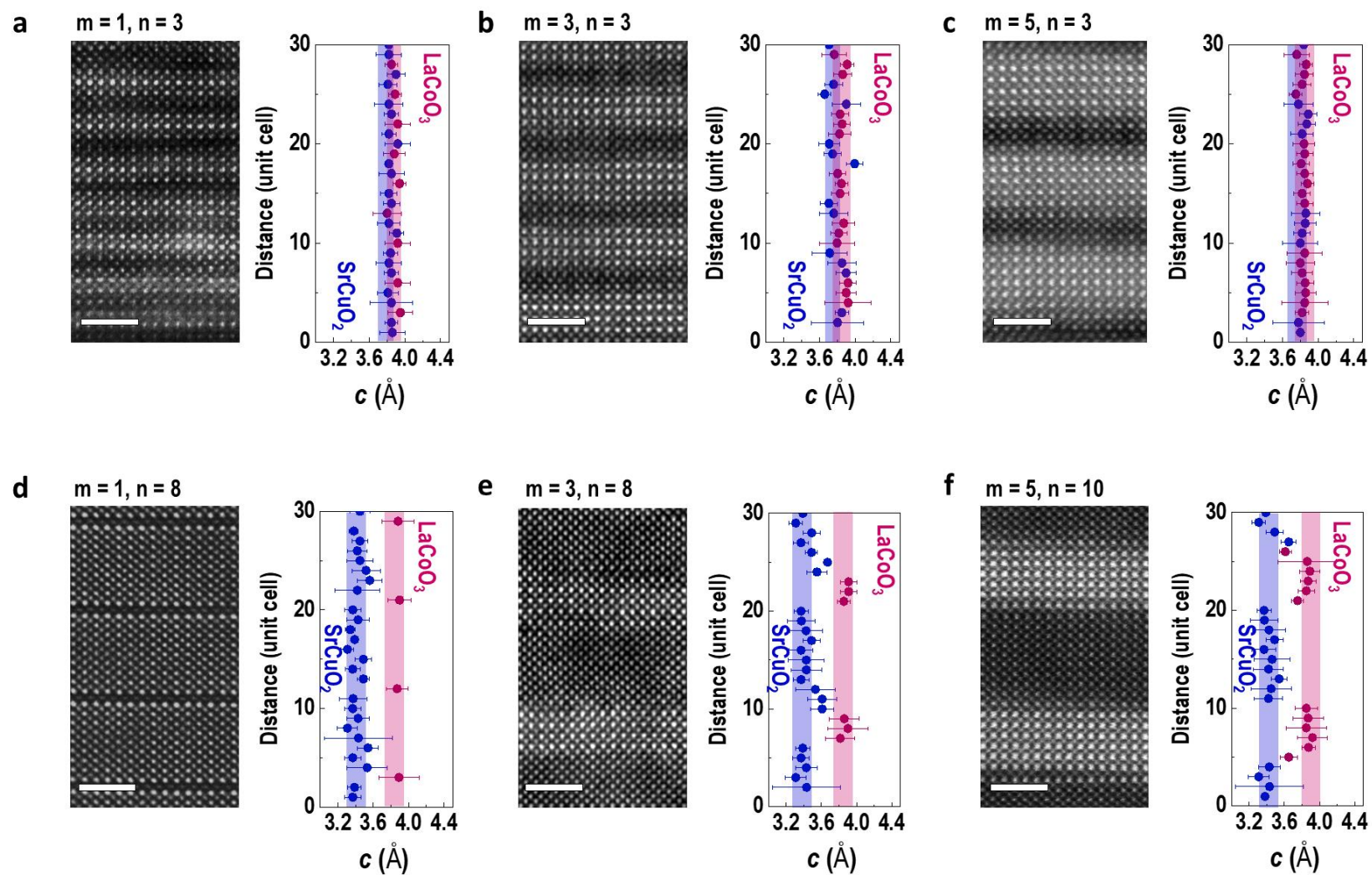
$[(\text{LaCoO}_3)_m/(\text{SrCuO}_2)_n]_{15}$ superlattices

Figure S5. Lower-magnification HAADF-STEM image and geometric phase analysis (GPA) of L_1S_8 . (a) HAADF-STEM image of L_1S_8 . Dark layers of LCO are seen between bright layers of P-SCO. At the bottom of image, we could see the STO substrates. Step edges from the substrates can be seen propagation through the films, as indicated by blue arrows. We find that there are approximately 20–50 nm continuous two-dimensional LCO sheets before encountering a step edge. We do not find any regions that may contain LCO double layers. However, we do see some regions (marked with yellow rectangles) that may contain small amount of reoriented structural defects. These LCO layers run at angles through the film that are not parallel to the direction of the electron beam, so in the projection image of the thin sample we may see the discontinuous LCO single layers. (b) and (c) In-plane and out-of-plane strain distribution within L_1S_8 , respectively. The GPA results reveal the uniformed in-plane lattice constants within both layers and substrates, consistent with the RSM results of the coherently grown films. The color contrast between left and right parts may attribute to the thickness difference of samples. We find that the strain states of superlattices vary slightly around these structural variations. We hypothesis that the misalignment of LCO at the step edges and the reoriented structural defects in the films may play an important role in the strain relaxation and accommodation of huge strain gradient ($> 10^8 \text{ m}^{-1}$) along the growth direction.

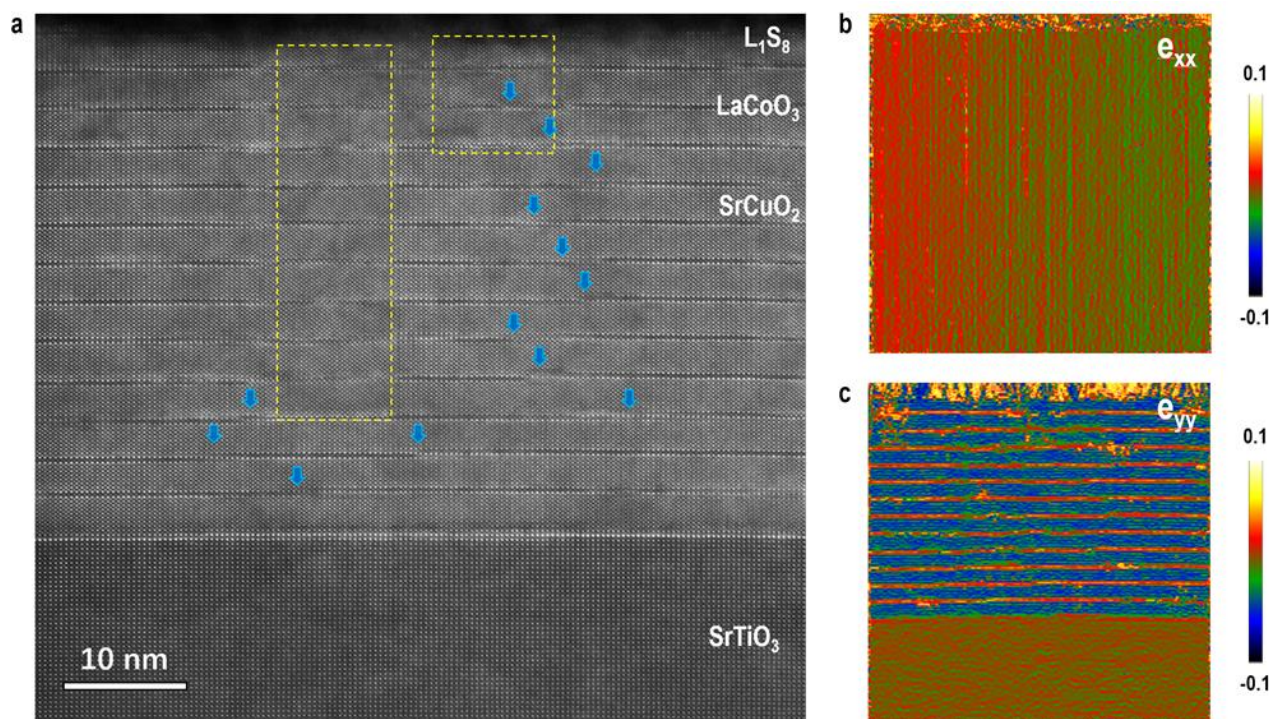


Figure S6. HAADF and EELS imaging collected from a representative region in L_3S_3 . (a) High magnification HAADF-STEM image from a selected region in L_3S_3 . The HAADF image is a little distorted due to the thermal drift during the image scanning. The LCO and C-SCO layers are marked in numbers, from which we could distinguish the individual layer. The colored panels show the integrated intensities of (b) La $M_{4,5-}$, (c) Co $L_{2,3-}$, (d) Cu $L_{2,3-}$ edges, respectively. (e) The color overlay of all elements' signals. (f) Elemental profiles obtained from the EELS imaging averaged across the whole images, from which we could identify both interfaces were atomically sharp with the LaO-CuO layer sequence. EELS results indicate the uniformity of elemental distribution within each layer. We found both interfaces do not exhibit significant intermixing inside the LCO layers. The chemical intermixing at the LCO-SCO interfaces is approximately single-unit-cell thick. The EELS signals from Cu $L_{2,3-}$ edges is relatively weak because the energy band (950-970 eV) is close to the spectrum upper limit.

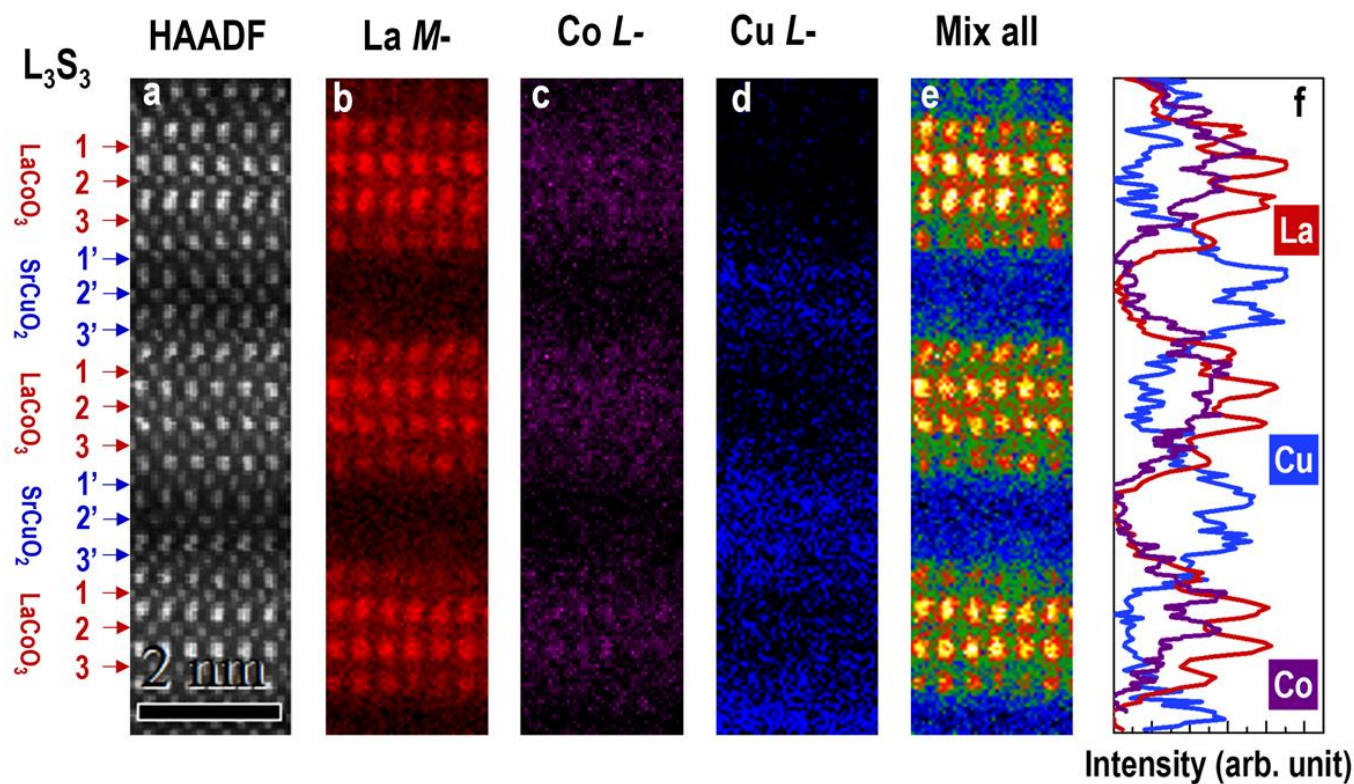


Figure S7. ABF-STEM images for L_3S_3 and L_3S_8 superlattices. (a) and (b) Cross-sectional ABF-STEM images for L_3S_3 and L_3S_8 superlattices, respectively. The ABF-STEM imaging is sensitive to the light atoms, providing a great opportunity to monitor the positions of the oxygen atoms with respect to the heavy atoms. Samples are imaged along the pseudocubic [100] zone axis. Insets show the sample geometries for the L_3S_3 and L_3S_8 superlattices. (c)-(f) Magnified ABF-STEM images for the regions indicated by blue (SCO) and purple (LCO) rectangles in (a) and (b). In both L_3S_3 and L_3S_8 superlattices, the Co atoms (purple) are surrounded by the oxygen atoms (blue) because the oxygen atoms occupy the face centers in the octahedral coordination of LCO. The arrangement of the oxygen atoms is quite different for the chain-type and the planar-type SCO layers. In the L_3S_3 superlattice, the columns containing heavy elements (Sr and Cu) together with oxygen atoms are clearly visible, as shown in (d), in agreement with the chain-type structure with a stacking ordering (...-SrO-CuO-SrO-...) in the SCO layers with a thickness below 5 u. c. However, the oxygen atoms in (F) are observed clearly in the Cu planes but no oxygen atom in the Sr planes of SCO layers. These results confirm directly the planar-type structure with stacking ordering (...-Sr-CuO₂-Sr-...) in the 8 u.c.-thick SCO layers in L_3S_8 superlattices. The ABF-STEM results from L_3S_3 and L_3S_8 superlattices provide a solid evidence on the thickness-dependent oxygen coordination transformation. [SR2] Another important observation is that the oxygen-rearrangement is throughout the entire thick SCO layers, not locates at the LCO-SCO interfaces solely.

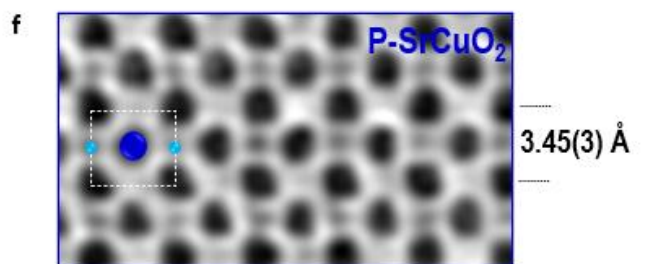
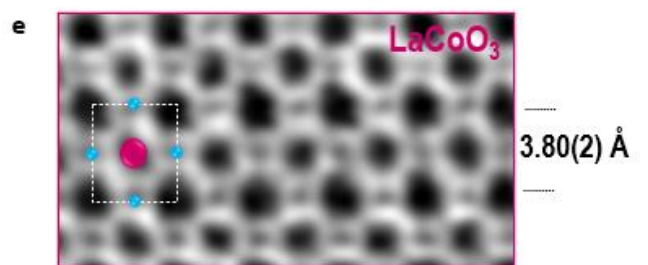
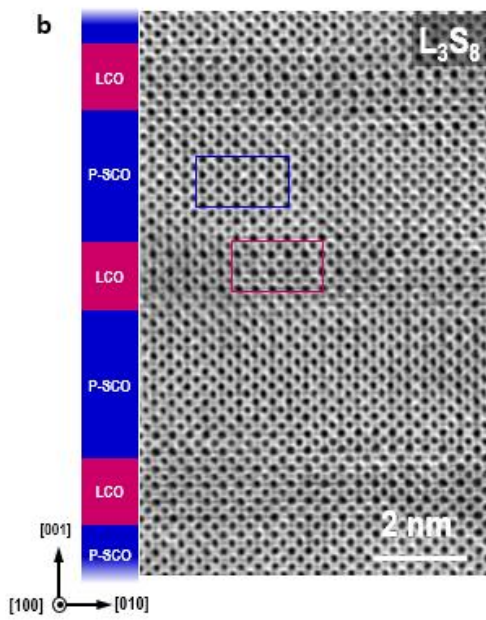
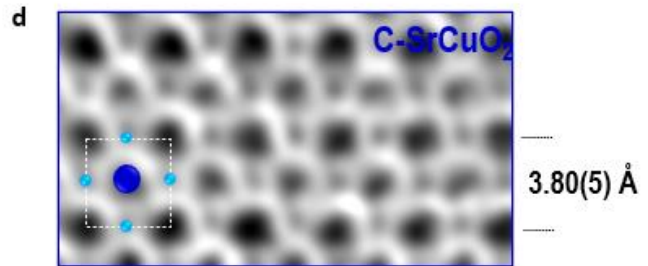
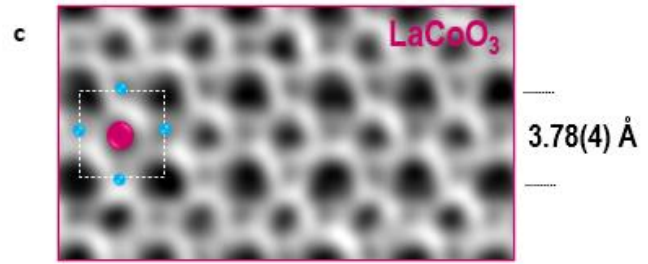
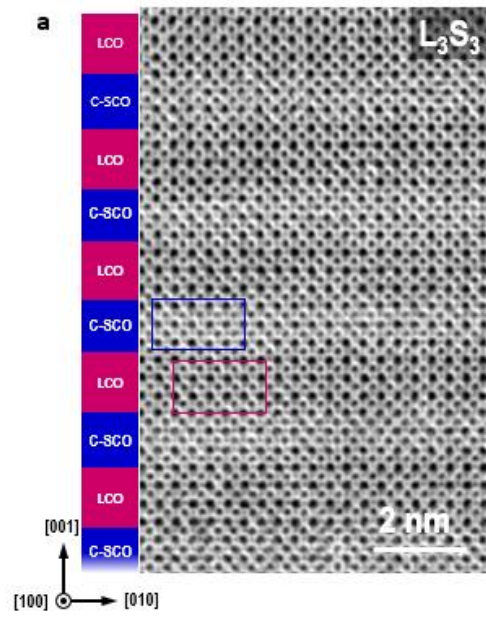


Figure S8. Electronic states of L_3S_3 and L_3S_8 superlattices. (a) and (b) Schematics of measurement setups when the incident beam has an incident angle (α) of 30° and 90° with respect to the sample's surface plane, respectively. XAS data were collected in total electron yield (TEY) mode. The electronic occupancy of Cu d orbitals was probed by changing incident angle with a fixed linearly polarized x-ray beam. When the x-ray beam was perpendicular to the sample's surface, as shown in (b), it reflects the orbital occupancy of Cu $d_{x^2-y^2}$ orbital directly. When the x-ray beam incident on the sample's surface with an angle of 30° , then the XAS signal contains the information from both $d_{x^2-y^2}$ ($I_{ip} = I_{90^\circ}$) and $d_{3z^2-r^2}$ [$I_{oop} = (I_{90^\circ} - I_{30^\circ}) \cdot \sin^2 30^\circ / \cos^2 30^\circ$] orbitals. As shown in (c), XAS($\alpha = 30^\circ$) and XAS($\alpha = 90^\circ$) share the similar intensity and trend for L_3S_3 superlattices. It suggests that the electron occupancy is nearly equal for in-plane and out-of-plane orbitals. The oxygen coordination of SCO in L_3S_3 superlattices is chain-type structure. By contrast, the intensity and peak energy of XAS($\alpha = 30^\circ$) is smaller than that of XAS($\alpha = 90^\circ$) in L_3S_8 superlattices [(d)], indicating that most of holes occupy the $d_{x^2-y^2}$ orbital. This result suggests the oxygen coordination of SCO in L_3S_8 superlattices is planar-type structure, well consistent with typical layered cuprate orbital configuration. [SR3] The reference spectra (black dashed lines) of Cu L -edges from $LaNiO_3$ - $SrCuO_2$ superlattices were provided for comparison. [SR4] We found both lineshape and peak positions of our spectra is identical to the reference samples, indicating the valence state of Cu keeps +2. (e) and (f) X-ray linear dichroism (XLD) for L_3S_3 and L_3S_8 superlattices, respectively (same as Figs. 1f and 1g). XLDs were calculated from $XLD = I_{oop} - I_{ip}$, where I_{ip} and I_{oop} is the corrected XAS intensity by considering the geometry of measurement setups. Large XLD observed in L_3S_8 superlattice emphasizes the large orbital polarization, compared to that of L_3S_3 superlattice. XLD results reinforce the predominant $d_{x^2-y^2}$ hole character and planar-type oxygen coordination in L_3S_8 superlattices, meanwhile the in-plane and out-of-plane orbitals in L_3S_3 superlattice are degenerated.

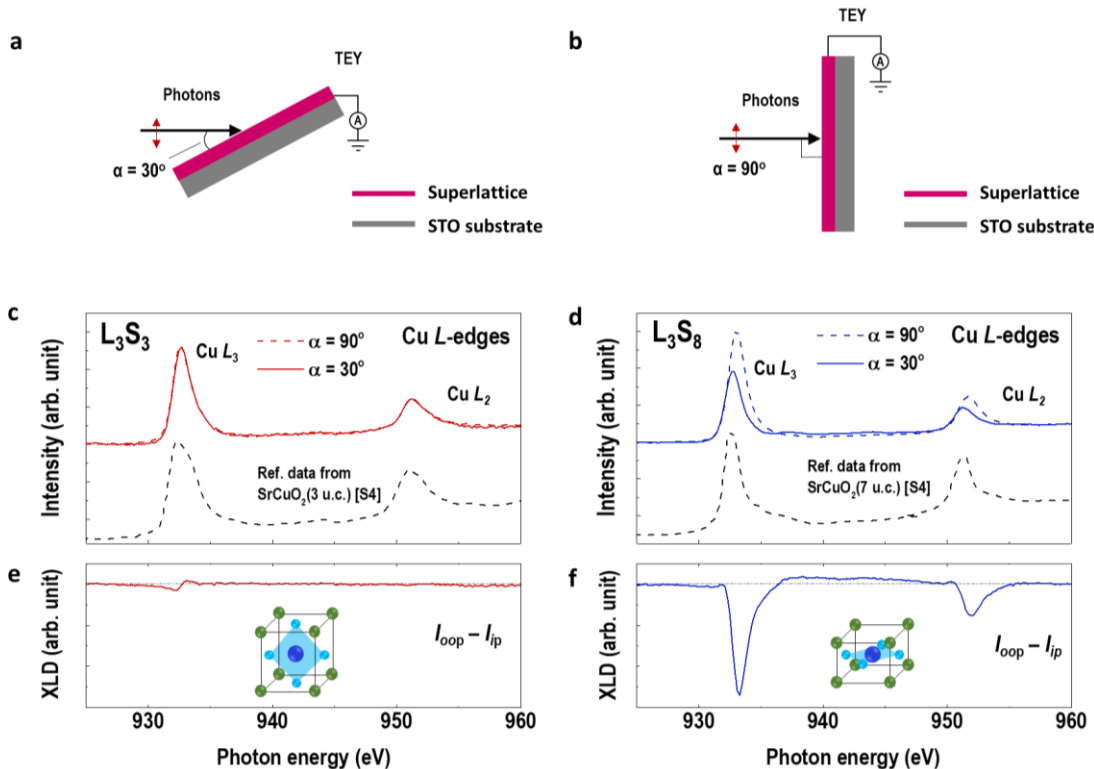


Figure S9. Magnetization characterizations. (a) M - H loops and (b) M - T curves for a 5 u.c.-thick LCO single layer, a 40u.c.-thick SCO single layer, and a L_5S_1 superlattice. The SCO thick film is not a ferromagnet at all temperatures. The LCO ultrathin layer, constrained by the STO substrate, possibly keeps a high-order symmetry – pseudotetragonal structure, exhibiting a low-spin state. This observation agrees with our earlier work on the symmetry-mismatch induced spin state transition in LCO ultrathin films. The layer-resolved magnetization probed by polarized neutron reflectometry indicates the LCO ultrathin films with a higher order symmetry exhibit a lower magnetization, whereas the film bulk part with a relaxed shear strain has a larger magnetization. [SR5] We observed a clear magnetic hysteresis loop in the L_5S_1 superlattice. The M - T curve at $\mu_0H = 1$ kOe shows a paramagnetic (PM)-ferromagnetic (FM) phase transition at Curie temperature (T_C) ~ 85 K, consistent with the T_C of ferromagnetic LCO films. [SR6-SR8]

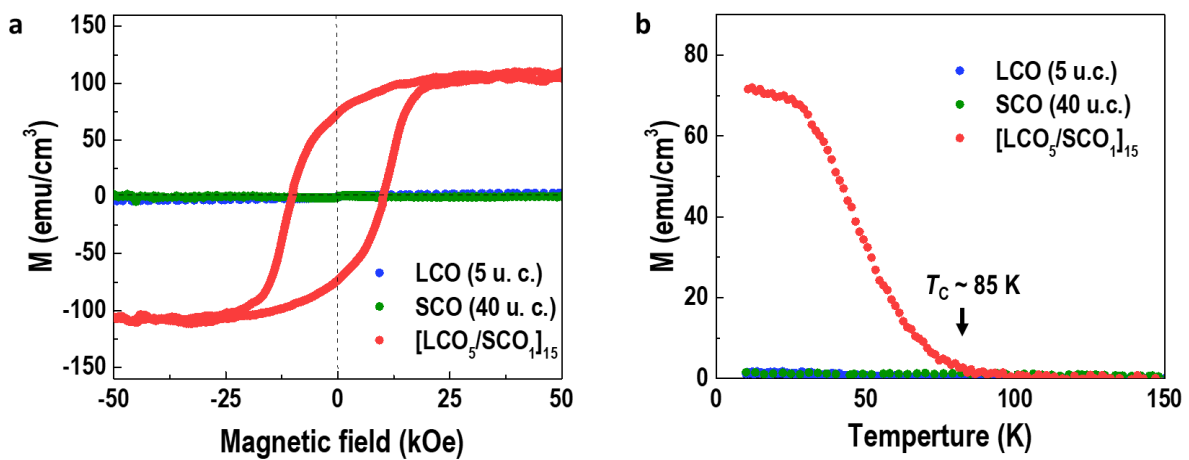


Figure S10. XRR curves of L_5S_1 and L_5S_{10} superlattices. The solid lines in (a) and (b) are the best fittings to the experimental data (open symbols). The frame of merits (FOM) in (a) and (b) yield 0.04 and 0.06, respectively. (c) and (d) X-ray scattering length density (SLD) depth profiles of L_5S_1 and L_5S_{10} superlattices, respectively. The total thickness of L_5S_1 superlattice is (37.5 ± 0.4) nm and the total thickness of L_5S_{10} superlattices is (79.1 ± 0.7) nm. The choice of superlattices' period is because the oxygen coordination of SCO layers in L_5S_1 superlattices is the chain-type structure, whereas the oxygen coordination of SCO layers in L_5S_{10} superlattices is the planar-type structure. The chemical compositions of the superlattices are used for the polarized neutron reflectivity (PNR) fittings in Figs. 3d-3e of main text and Fig. S9. The XRR curves were fitted using GenX software. [SR9]

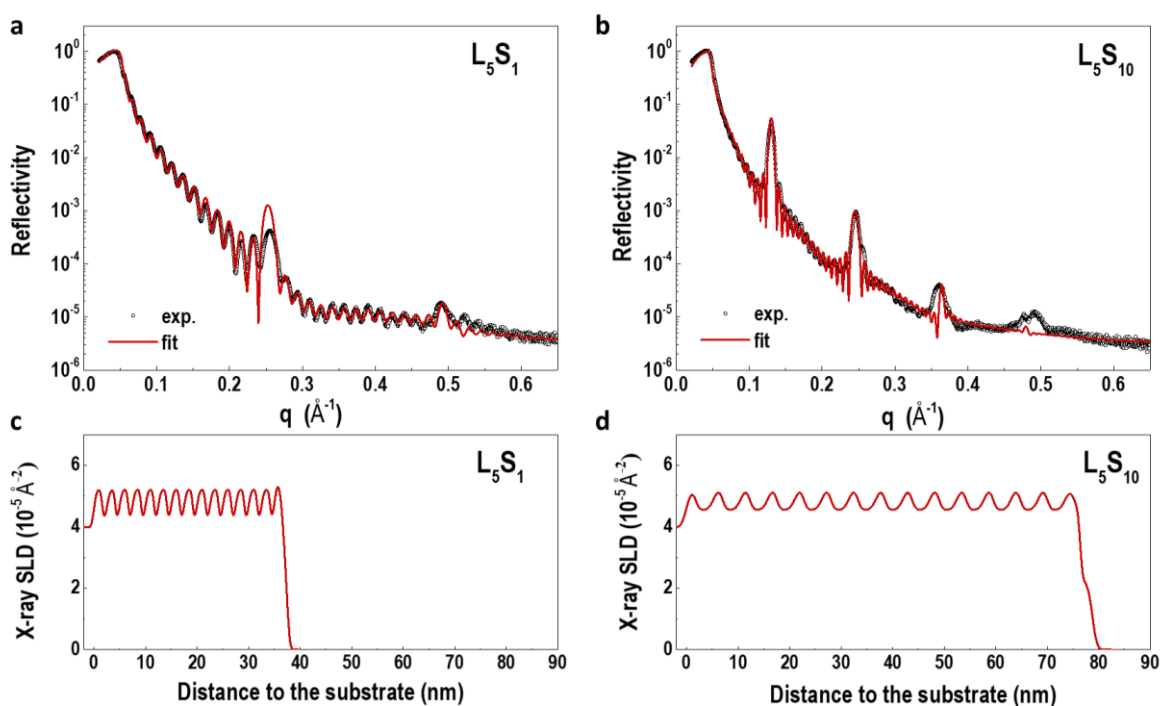


Figure S11. PNR measurements on a L_5S_{10} superlattice. (a) Measured (open symbols) and fitted (solid color lines) neutron reflectivities for spin-up (R^+) and spin-down (R^-) polarized neutron beams are plotted as a function of wave vector q ($= 4\pi \cdot \sin\theta/\lambda$), where θ is the incident angle and λ is the wavelength of neutron beam. The PNR measurements were taken at 10 K after field-cooling at $\mu_0 H = 3$ T. The magnetic field was applied along the in-plane direction and kept throughout the measurements. (b) The spin asymmetry (SA) derived from the neutron reflectivity and was calculated by $(R^+ - R^-)/(R^+ + R^-)$. Solid line is the best fit to the experimental data. (c) Magnetization (magnetic scattering length density, $mSLD$) depth profile of a L_5S_{10} superlattice. The SCO layers exhibit zero magnetic moment, in agreement with the result from L_5S_1 superlattice (Fig. 3). The magnetizations of the bottom (~ 35.2 emu/cm³) and top (~ 70 emu/cm³) LCO layers are slightly different from the middle LCO layers due to the different boundary conditions. The averaged magnetization of LCO layers in L_5S_{10} superlattice is 59.2 emu/cm³, which is much smaller than the magnetization of LCO layers in L_5S_1 superlattice (~ 115 emu/cm³) (Fig. 3d of main text). The PNR results are consistent with the VSM magnetometry measurements, indicating a strong modulation of ferromagnetism in LCO layers by oxygen coordination of SCO layers.

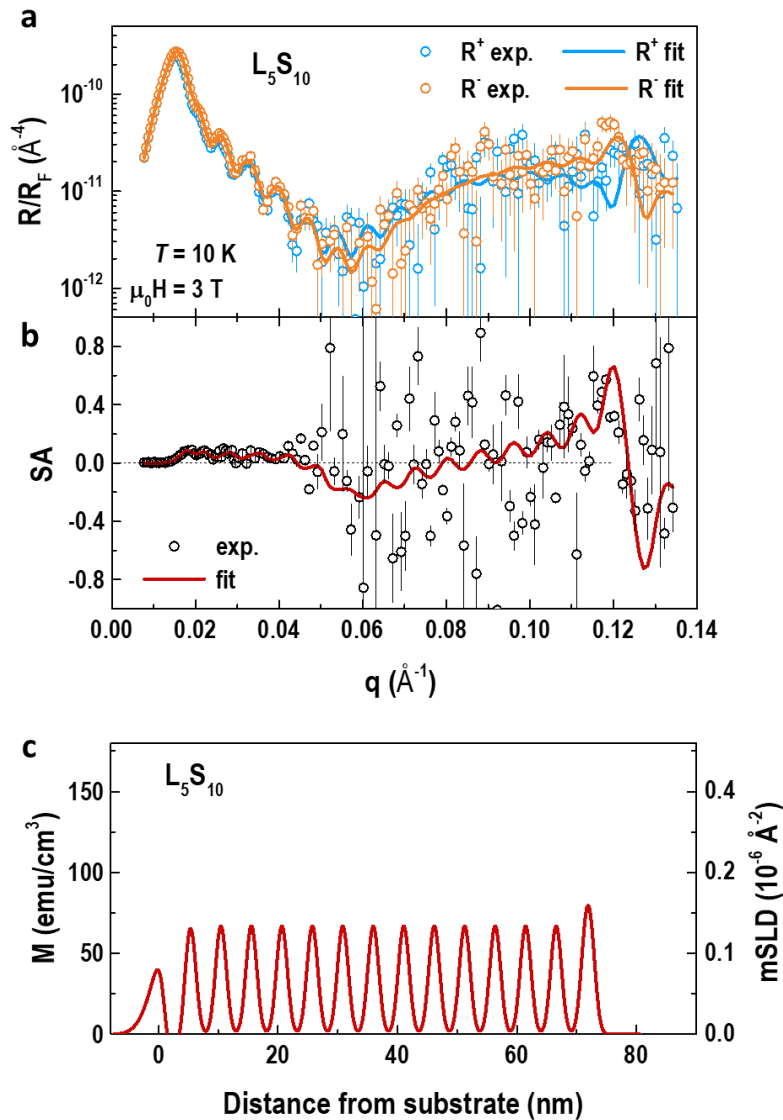


Figure S12. Magnetization characterizations of L_mS_1 superlattices. (a) M - H loops for L_mS_1 ($1 \leq m \leq 10$) superlattices. Data were taken at 10 K with applied in-plane magnetic fields. All samples exhibit clear hysteresis loops, indicating a ferromagnetic nature. (b) and (c) show the coercive fields (H_C) and saturation magnetizations (M_S) plots against the thickness of LCO layer (in unit cell), respectively. For the L_1S_1 superlattice, the M_S used in the plots is the magnetization derived at $\mu_0H = 5$ T because the magnetization of L_1S_1 superlattice is not saturated at the maximum magnetic field. We observed a clear drop when the LCO layer thickness exceeds 5 u. c., suggesting the effects from the oxygen coordination of SCO layer decreases significantly above this thickness limit. Thickness dependence of magnetization excludes the effect of chemical intermixing at the interfaces. If the Sr (or Cu) doping into the LCO layers plays a dominating role in the induced magnetization, then it should have equivalent effect on all the L_mS_1 superlattices. However, our VSM magnetometry measurements did not support this exceptional scenario.

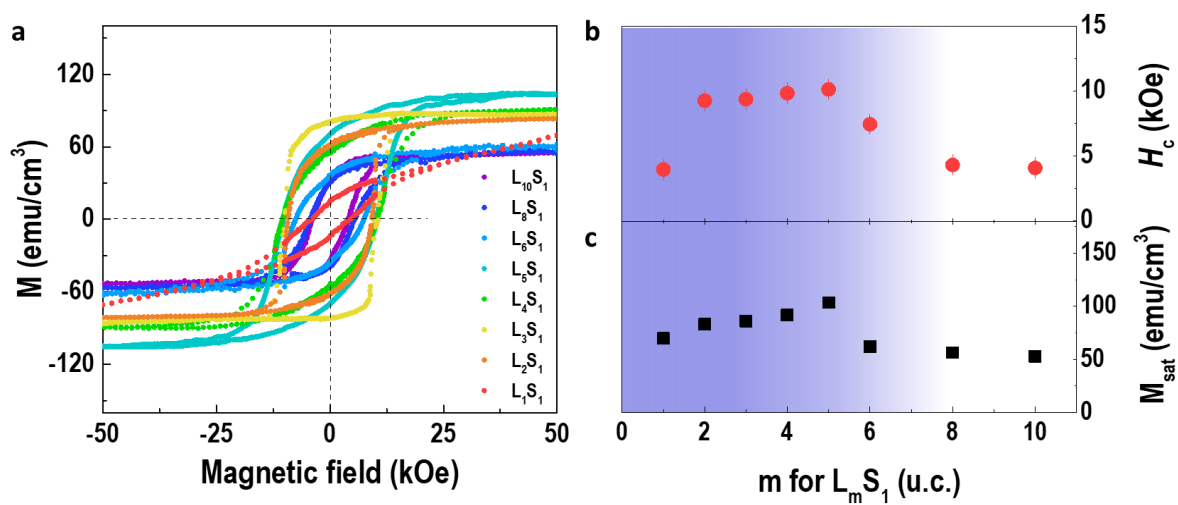
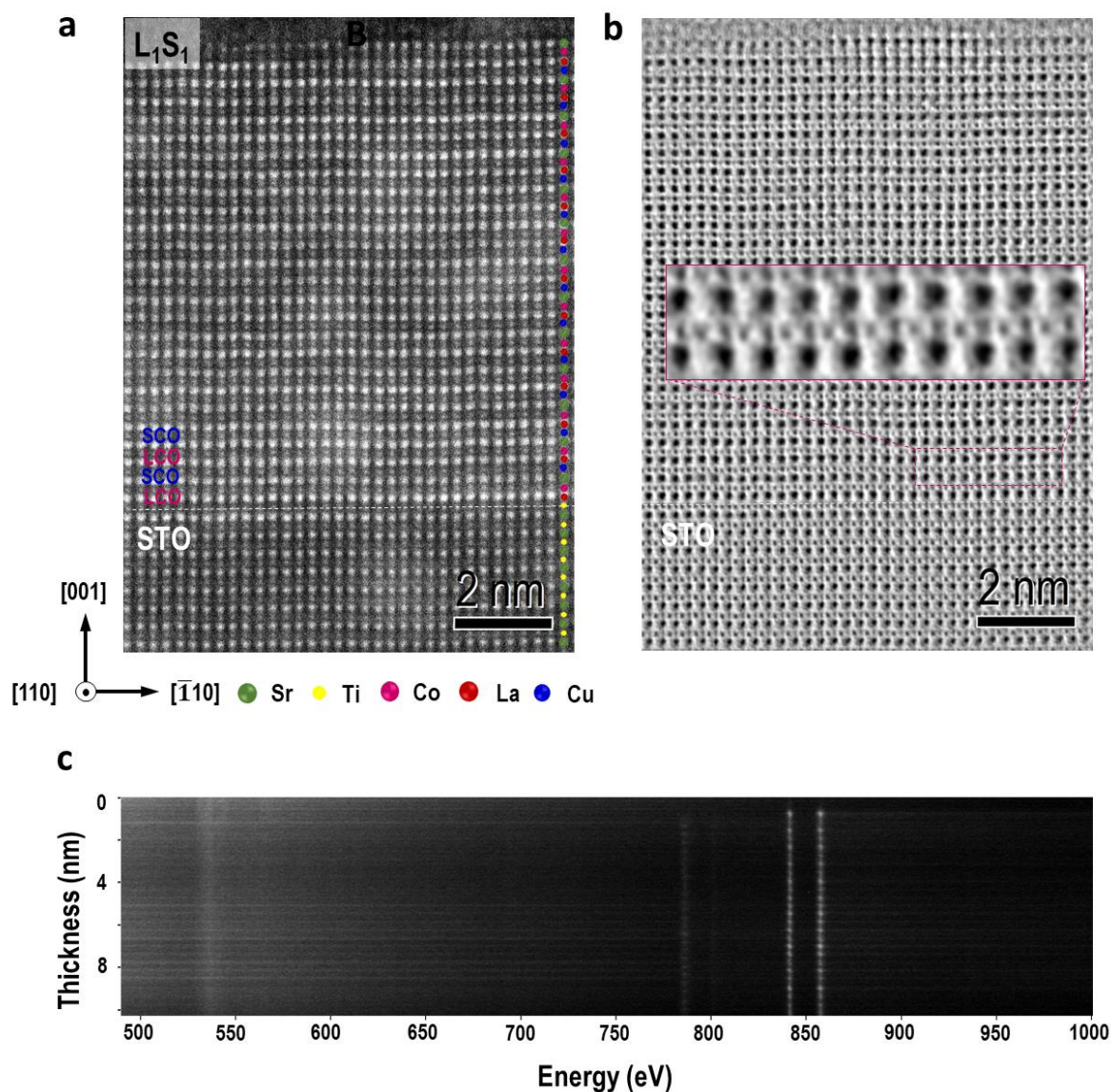


Figure S13. Microstructural characterizations of a L_1S_1 superlattice. (a) HAADF-STEM and (b) ABF-STEM images of a L_1S_1 superlattice. The image was taken along the pseudocubic $[110]$ zone axis. The positions of atoms were marked in the ABF-STEM image. Dashed lines indicate the interface between the STO substrate and L_1S_1 superlattice. Inset of (b) shows the magnified ABF image for the region indicated by a purple rectangle, where marked the position of an LCO layer. We could observed the the bonding angle $\beta_{\text{Co-O-Co}}$ is smaller than 180° , indicating the distorted octahedral. (c) Layer-resolved full EELS spectra of a L_1S_1 superlattice. Three features at around 525, 780, and 850 eV are the energy bands of oxygen, cobalt, and lanthanum, respectively. The signal from copper is too low to be resolved from the noise. Each bright spot along the thickness axis represents the position of corresponding atom. HAADF-STEM images and EELS maps reveal an extreme high-quality superlattice with sharp interfaces. The thicknesses of LCO and SCO layers are equivalent of one-unit-cell in thickness. The chemical intermixing is minimum and has limited effects on the magnetic properties of our superlattices.



Supplementary Note 1. Electronic states of LCO in the superlattices

The electronic state of LCO layers in the L_mS_n superlattices was characterized by elemental specific XAS in total electron yield (TEY) mode with linearly polarized x-rays with variable incident angles. The XAS measurements at Co L -edges were taken at zero magnetic field to exclude the possible linear dichroism from the orbital anisotropy induced by magnetic percolations. The line shape of Co L -edges, similar to the Fig. 3b, confirms that the LCO layers in the superlattices are oxygen stoichiometric with negligible Co^{2+} ions mixed in the LCO films. Figs. S12a and S12b show the XLD at Co L -edges for L_3S_3 and L_3S_8 superlattices, respectively. The calculation method for XLD was discussed previously in the captions of Fig. S6. The electronic occupancy of Co d orbitals can be illustrated directly by comparing the difference between two XLDs. First of all, both XLDs show negative values, i.e. $(I_{ip} - I_{oop}) < 0$, suggesting the occupation of d electrons in the $d_{x^2-y^2}$ orbital is larger compared to the $d_{3z^2-r^2}$ orbital. Secondly, the peak intensity of XLD spectra for L_3S_3 superlattices is remarkably larger than that of L_3S_8 superlattices, indicating the orbital polarization for the L_3S_3 superlattices is much larger than that of L_3S_8 superlattices. Both XRD and STEM results indicate an elongation of LCO unit cells along the out-of-plane direction in the L_3S_8 superlattices, resulting in a slightly reduced energy in $d_{3z^2-r^2}$ orbital. Therefore, the tetragonally distorted lattice will lead to a distortion of CoO_6 octahedra towards leveling the Co-O-Co bonding angle, i. e. the e_g band width (W) increases as $W \propto \cos(\pi - \beta)/d^{3.5}$, thus the electrons will move back to the t_{2g} orbitals. The XLD results further prove the spin state of Co^{3+} ions in L_3S_8 superlattices is lower than those in L_3S_3 superlattices, supporting the observed magnetization data and microstructural observations by STEM.

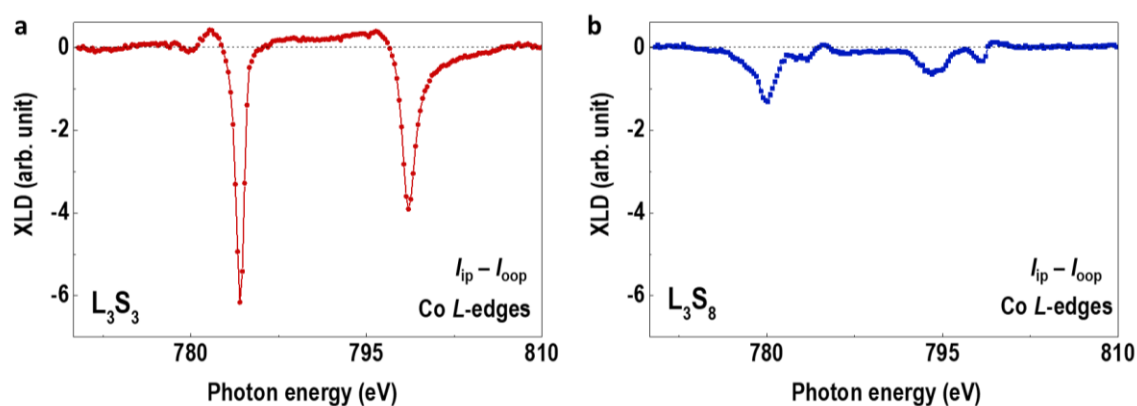


Figure S14. Electronic states of LCO in LCO/SCO superlattices. (A) and (B) XLDs at Co L -edges for the L_3S_3 and L_3S_8 superlattices, respectively.

Supplementary Note 2. Effect of tetrahedra on the electronic configuration in LCO layers

The electronic configuration of $3d$ transition metal orbitals would be visualized as electron bands, as shown in Fig. S13a. The ligand field of molecular orbitals splits into the threefold degenerate nonbonding t_{2g} and twofold degenerate antibonding e_g bands. In the Co-O orbitals, the spin state of Co^{3+} ion depends strongly on the oxygen coordination, i.e. octahedral vs. tetrahedral structure, in a unit cell. For the octahedral ligand field, the energy of e_g bands ($d_{x^2-y^2}$ and $d_{3z^2-r^2}$) is higher than that of t_{2g} bands (d_{xy} , d_{yz} , and d_{xz}). The six free electrons in the Co^{3+} ions will occupy the three lowest energy bands in the undistorted octahedral structure. Thus, the Co^{3+} ion is in a low-spin state, exhibiting no net spin moment ($S = 0$). However, in the tetrahedral ligand case, the energy band structure reverses its aligned order. The e_g bands have a lower energy than those of t_{2g} bands. Four free electrons will occupy the e_g bands, then the other two free electrons will be on the t_{2g} bands, resulting in a net spin moment ($S = 1$). Therefore, one may ask whether the large magnetization observed in the L_1S_1 superlattices is a result of tetrahedral ligand structure or not?

Figs. S13b and S13c illustrate the schematic of atomic sublayers in the L_1S_1 and L_1S_n ($n \geq 5$) superlattices, respectively. The atomic structures of sublayers are obtained from the HAADF-STEM and ABF-STEM images. In both cases, the experimental results support the oxygen coordination in the L_1S_n superlattices is the octahedral structure, not the tetrahedral structure. Therefore, the large magnetization in the ultrathin LCO layers can not be attributed to the electronic configuration transformation from an octahedra to a tetrahedra. We believe the experimental evidence supports that the structural distortion in the CoO_6 octahedra triggers the spin state transition in Co^{3+} ions, resulting in the observed ferromagnetism in one-unit-cell thick LCO layers.

Supplementary Note 3. Polar catastrophe effect at the LCO/SCO interfaces

Polar discontinuity at the oxide interfaces has tremendous effect in the magnetic properties of ultrathin layers. [SR10, SR11] The uncompensated interfacial charges will modify the chemical composition and induce large lattice distortions. Therefore, detailed analysis of polar-nonpolar interfaces is important in understanding the observed ferromagnetism in a L_1S_1 superlattice. From HAADF-STEM images (Fig. 5a and Fig. S11), we found that the stacking order of sublayers in a L_1S_1 superlattice is ...-CuO-LaO-CoO₂-SrO-CuO-.... In the SCO layers, the natural sublayers (CuO and SrO) are charge neutral, i.e. the nominal charge cation and anion in each plane cancels each other. In the LCO layers, the natural sublayers (LaO and CoO₂) are alternative charged with $+1e^-$ and $-1e^-$, respectively. When these two sublattices join as the heterointerfaces, the electronic states in the superlattices will spontaneously reconstruct. This requires an interfacial dipole that causes the electric field to oscillate around zero and the potential remains finite. From the Fig. S14, the electronic configuration of Co³⁺ ion is not changed. The potential divergence for the CuO-LaO-CoO₂-SrO interfaces can be avoided by removing an electron from the SrO plane and filling an electron in the CuO plane. The upper free surface is not shown here, but in the simple model the uppermost CuO plane would be charge neutral, which bring the electric field and potential back to zero at the surface. The divergence for the bottom interface between TiO₂ and LaO (LCO/STO interface) can be neutralized by filling an electron into TiO₂ sublayer in the form of oxygen vacancies. In fact, the actual surface and superlattice/substrate reconstructions might be more complicated. [SR12] Here, with this simple model, we explain the polar catastrophe does not affect the magnetic ground state of LCO ultrathin layers with a thickness of one-unit-cell. Therefore, the interfacial charge effect in the L_1S_1 superlattices can be excluded.

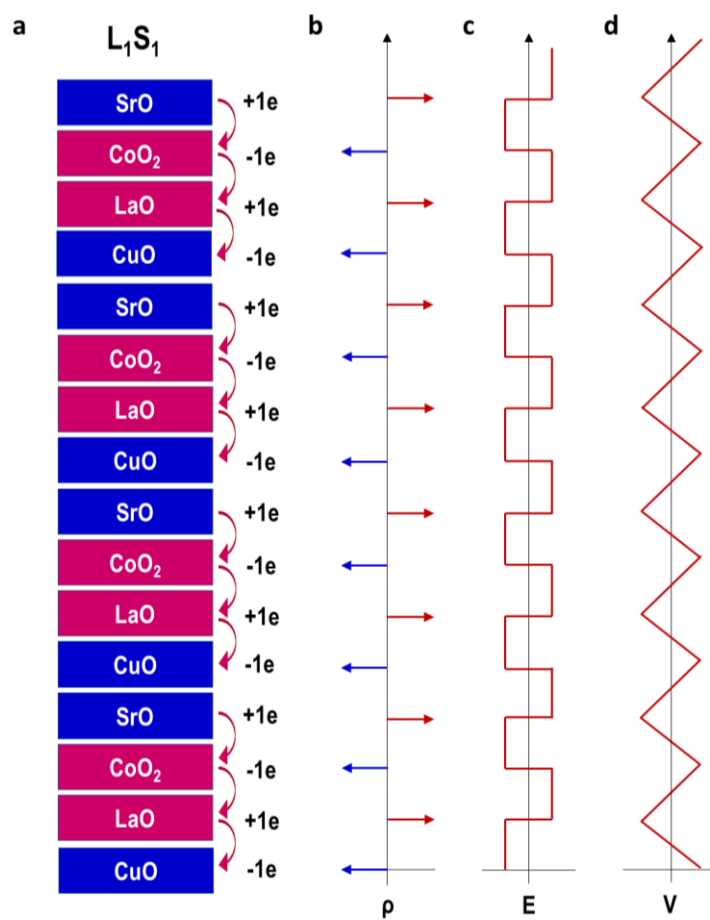


Figure S16. Polar interfaces and electronic reconstruction model for L_1S_1 superlattices. (A) Sample structure and net charges in the atomic sublayers. (B) Net charge, ρ , (C) electric-field, E , and electrical potential, V as a function of film thickness.

Supplementary References

- [SR1] Z. Zhong, *et al.*, Prediction of thickness limits of idea polar ultrathin films, *Phys. Rev. B* **85**, 121411 (R) (2012).
- [SR2] D. Samal, *et al.*, Experimental evidence for oxygen sublattice control in polar infinite layer SrCuO₂, *Phys. Rev. Lett.* **111**, 096102 (2013).
- [SR3] J. Kanamori, Superexchange interaction and symmetry properties of electron orbitals, *J. Phys. Chem. Solids* **10**, 87-98 (1959).
- [SR4] Z. Liao, *et al.*, Large orbital polarization in nickelate-cuprate heterostructures by dimensional control of oxygen coordination, *Nat. Commun.* **10**, 589 (2019).
- [SR5] E. J. Guo, *et al.*, Exploiting symmetry-mismatch to control magnetism in a ferroelastic heterostructure, *Phys. Rev. Lett.* **122**, 187202 (2019).
- [SR6] D. Fuchs, *et al.*, Tuning the magnetic properties of LaCoO₃ thin films by epitaxial strain, *Phys. Rev. B* **77**, 014434 (2008).
- [SR7] W. S. Choi, *et al.*, Strain-induced spin states in atomically ordered cobaltites, *Nano Lett.* **12**, 4966 (2012).
- [SR8] E. J. Guo, *et al.*, Switchable orbital polarization and magnetization in strained LaCoO₃ films, *Phys. Rev. Mater.* **3**, 014407 (2019).
- [SR9] M. Björck and G. Andersson, *J. Appl. Cryst.*, **40**, 1174-1178 (2007).
- [SR10] M. Huijben, *et al.*, Critical thickness and orbital ordering in ultrathin La_{0.7}Sr_{0.3}MnO₃ films, *Phys. Rev. B* **78**, 094413 (2008).
- [SR11] H. Boschker, *et al.*, Preventing the Reconstruction of the Polar Discontinuity at Oxide Heterointerfaces, *Adv. Funct. Mater.*, **22**, 2235 (2012).
- [SR12] N. Nakagawa, *et al.*, Why some interfaces cannot be sharp, *Nat. Mater.* **5**, 204 (2006).